

SEMI-ANALYTIC PINN METHODS FOR BOUNDARY LAYER PROBLEMS IN A RECTANGULAR DOMAIN

GUNG-MIN GIE¹, YOUNGJOON HONG², CHANG-YEOL JUNG³, AND TSELMUUN MUNKHJIN³

ABSTRACT. Singularly perturbed boundary value problems pose a significant challenge for their numerical approximations because of the presence of sharp boundary layers. These sharp boundary layers are responsible for the stiffness of solutions, which leads to large computational errors, if not properly handled. It is well-known that the classical numerical methods as well as the Physics-Informed Neural Networks (PINNs) require some special treatments near the boundary, e.g., using extensive mesh refinements or finer collocation points, in order to obtain an accurate approximate solution especially inside of the stiff boundary layer. In this article, we modify the PINNs and construct our new semi-analytic SL-PINNs suitable for singularly perturbed boundary value problems. Performing the boundary layer analysis, we first find the corrector functions describing the singular behavior of the stiff solutions inside boundary layers. Then we obtain the SL-PINN approximations of the singularly perturbed problems by embedding the explicit correctors in the structure of PINNs or by training the correctors together with the PINN approximations. Our numerical experiments confirm that our new SL-PINN methods produce stable and accurate approximations for stiff solutions.

CONTENTS

1. Introduction	1
2. Boundary layer analysis	3
2.1. Non-characteristic boundary case ($b_1 > 0, b_2 > 0$)	4
2.2. Characteristic boundary case ($b_1 > 0, b_2 = 0$)	7
3. Numerical experiments	10
3.1. Non-characteristic boundary case ($b_1, b_2 > 0$)	12
3.2. Characteristic boundary case ($b_1 > 0, b_2 = 0$)	15
4. Conclusion	19
Acknowledgments	20
References	20

1. INTRODUCTION

We employ the neural network architectures to approximate effectively the solutions of various 2D singularly perturbed elliptic boundary value problems in a rectangular

Date: December 12, 2023.

domain $\Omega = (0, 1)^2$. More precisely, we consider,

$$\begin{cases} -\varepsilon\Delta u - \mathbf{b} \cdot \nabla u = f, & \text{in } \Omega, \\ u = 0, & \text{on } \partial\Omega, \end{cases} \quad (1.1)$$

where $0 < \varepsilon \ll 1$ is a small perturbation parameter. The given functions $\mathbf{b} = (b_1(x, y), b_2(x, y))$ and $f = f(x, y)$ are assumed to be smooth as much as needed for the analysis and computations performed in this article.

Singularly perturbed boundary value problems, e.g., the one described by equation (1.1) above, are known to generate the so-called boundary layer, which is a thin region near the boundary of the domain where the solution exhibits a sharp transition. The mathematical theory of singular perturbations and boundary layers has been extensively studied in the literature, and several books and papers have been written on the subject, including [15, 18, 27, 33].

From the scientific computation's point of view, approximating stiff solutions to any singular perturbation problem is well-known to be a challenging task because the stiffness of the solution, especially inside the boundary layer, causes a large computational error. Most of the traditional numerical methods, such as finite element or finite volume methods, often require massive mesh refinements near the boundary in order to achieve a sufficient accuracy of numerical solutions, but the computational cost for this type of refinements is highly expensive with respect to the size of the small perturbation parameter.

Compared to the traditional methods, some semi-analytical methods have been proposed to compute the solutions more efficiently and effectively, such as the ones presented in [6, 10, 11, 12, 16, 19, 20]. These methods enrich the basis of traditional numerical methods by adding a global basis function, called *correctors*, which describes the singular behavior of the solution inside the boundary layer. By enriching the basis, these methods can capture the sharp transition of the solution without requiring massive mesh refinements near the boundary. The semi-analytic methods have proven to be highly efficient in solving singularly perturbed problems, and they have been successfully applied in various applications.

In our paper, we use the neural network methods, in particular the Physics-Informed Neural Networks (PINNs) to solve the singularly perturbed problems. Neural networks offer a novel approach to approximating solutions to differential equations using a compositional structure instead of an additive one. This approach allows for analytical expression of the solution, eliminating the need for interpolation. The formulation of the loss function is straightforward, and the additional effort required for problem-dependent factors is minimal. The method is mesh-free and generally applicable [2, 3, 5, 17, 22, 23, 24, 29, 31, 34, 35]. However, there is still a lack of conclusive results regarding convergence speed and approximation accuracy.

Raissi et al.'s PINNs [30] drew inspiration from earlier works by e.g. Lagaris et al. [26] and they expanded on existing concepts and introduced fundamentally new approaches, including a discrete time-stepping scheme that optimizes the predictive power of neural networks. However, while PINNs have shown promising results in

various applications, such as fluid dynamics and solid mechanics, they are known to suffer from the spectral bias phenomenon [4, 28]. The spectral bias phenomenon refers to the tendency of neural networks to learn low-frequency features before high-frequency features. In other words, the network tends to learn coarse features before fine details, which can result in a biased representation of the solutions. It is also known that the PINNs often fail to solve the solutions exhibiting multi-scale structures [25]. The PINNs are particularly problematic when dealing with singularly perturbed problems, where the solution can vary rapidly over small scales in the domain, i.e., high-frequency solutions. In these cases, the neural network may not have sufficient resolution or detail to accurately capture the solution, leading to inaccurate results [7, 32, 36]. Recently, the boundary-layer PINNs are proposed to utilize the matching techniques of the outer and inner layer solutions based on singular perturbation theory [1].

To overcome the spectral bias phenomenon or to solve rapidly varying solutions, we combine the semi-analytic methods with the PINNs (e.g., see [9]). In fact, we obtain our new SL-PINN (singular layer PINN) approximations for the singularly perturbed problems by embedding the explicit correctors in the structure of PINNs or by training the correctors together with the PINN approximations. For this process, in Section 2, we first perform the boundary layer analysis for the problem (1.1), and study the asymptotic behavior of the solution. In Section 3, we use the analytic results to modify the PINNs and construct our new SL-PINNs suitable for the singular perturbation problem (1.1). Numerical computations of the SL-PINNs are presented as well to verify that our novel SL-PINNs capture well the sharp transition of the stiff solution and hence produce a good approximation.

2. BOUNDARY LAYER ANALYSIS

In this section, we investigate the boundary layer of the singularly perturbed convection-diffusion problem(1.1) in a rectangular domain with corners. Depending on the direction of the convection vector \mathbf{b} , the solution to (1.1) exhibits a distinct behavior near each boundary and corner of the rectangular domain Ω . Hence we consider two different cases in this article:

- (1) $b_1(x, y) > 0$ and $b_2(x, y) > 0$ in Ω (*Non-characteristic boundary case*)
- (2) $b_1 > 0$ and $b_2 = 0$ in Ω (*Characteristic boundary case*)

Especially when a portion of the boundary is characteristic, i.e., the convection vector \mathbf{b} is parallel to that portion of the boundary like the case 2 above, the boundary layers of (1.1) associated with the two sides sharing the corner may interact with each other as well as the corner singularity; see, e.g., [8, 33, 15, 13, 14] that demonstrate the diversity and complexity of the boundary layers in a rectangle.

For the boundary layer analysis below, we introduce and use the following norms,

$$\|u\|_{L^2(\Omega)} = \left(\int_{\Omega} |u|^2 dx dy \right)^{1/2}, \quad (2.1)$$

$$\|u\|_\varepsilon = \|u\|_{L^2(\Omega)} + \sqrt{\varepsilon} \|\nabla u\|_{L^2(\Omega)}. \quad (2.2)$$

2.1. Non-characteristic boundary case ($b_1 > 0, b_2 > 0$). When the boundary is non-characteristic with $b_1 > 0, b_2 > 0$, the flow associated with (1.1) is moving in across the boundaries at $x = 1$ and $y = 1$. Hence, by setting $\varepsilon = 0$ in (1.1) and imposing the so-called *inflow boundary condition* at $x = 1$ and $y = 1$, we find the equation for the limit solution u^0 as

$$\begin{cases} -b_1 \frac{\partial u^0}{\partial x} - b_2 \frac{\partial u^0}{\partial y} = f, & \text{in } \Omega, \\ u = 0, & \text{at } x = 1 \text{ or } y = 1. \end{cases} \quad (2.3)$$

The well-posedness and regularity results for the problem (2.3) can be verified by using the method of characteristics. We assume hereafter that the data \mathbf{b} and f are smooth enough so that the limit solution u^0 is sufficiently regular for the boundary layer analysis below.

Now, to study the asymptotic behavior of u^ε (solution of (1.1)) as $\varepsilon \rightarrow 0$, we first notice that $u - u^0 = 0$ on $x = 1$ or $y = 1$, but

$$u - u^0 \neq 0 \text{ along the boundaries at } x = 0 \text{ and } y = 0. \quad (2.4)$$

Hence we expect that the so-called *ordinary boundary layers* occur near $x = 0$ and $y = 0$ (see Fig. 2.1 below). To resolve this inconsistency, we construct sequentially below a number of correctors as

- u^0 : corresponding limit solution defined in (2.3),
- θ_B : ordinary boundary layer corrector (OBL) near the bottom boundary at $y = 0$,
- θ_L : ordinary boundary layer corrector (OBL) near the left boundary at $x = 0$,
- η : corner boundary layer corrector (CBL) that manages the interaction between θ_B and θ_L near the corner at $(0, 0)$.

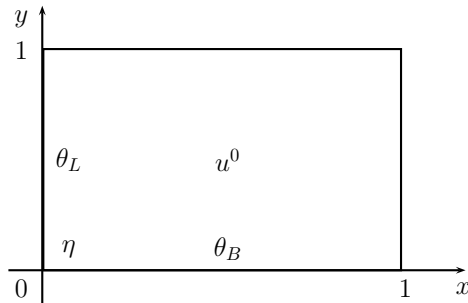


FIGURE 2.1. Limit solution, and ordinary and corner boundary layer correctors

We first introduce smooth cut-off functions near the left and bottom boundaries in the form,

$$\sigma_B(y) = \begin{cases} 1, & 0 \leq y \leq 1/8, \\ 0, & y \geq 1/4, \end{cases} \quad \sigma_L(x) = \begin{cases} 1, & 0 \leq x \leq 1/8, \\ 0, & x \geq 1/4. \end{cases} \quad (2.5)$$

To resolve the discrepancies of $u - u^0$ at $y = 0$, we write an asymptotic equation for the ordinary boundary layer near $y = 0$,

$$\begin{cases} -\varepsilon \frac{\partial^2 \bar{\theta}_B}{\partial y^2} - b_2(x, 0) \frac{\partial \bar{\theta}_B}{\partial y} = 0, \\ \bar{\theta}_B = -u^0(x, 0), & \text{at } y = 0, \\ \bar{\theta}_B \rightarrow 0, & \text{as } y \rightarrow \infty. \end{cases} \quad (2.6)$$

The explicit expression of $\bar{\theta}_B$ is readily available as

$$\bar{\theta}_B = -u^0(x, 0) \exp\left(-b_2(x, 0) \frac{y}{\varepsilon}\right). \quad (2.7)$$

Then we define the ordinary boundary layer corrector θ_B in the form,

$$\theta_B = \sigma_B(y) \bar{\theta}_B. \quad (2.8)$$

Using (2.6) - (2.8), we find that the ordinary boundary layer corrector θ_B satisfies the equation,

$$\begin{cases} -\varepsilon \frac{\partial^2 \theta_B}{\partial y^2} - b_2(x, 0) \frac{\partial \theta_B}{\partial y} = -\varepsilon \sigma'_B \frac{\partial \bar{\theta}_B}{\partial y} - \varepsilon \sigma''_B \bar{\theta}_B - b_2(x, 0) \sigma'_B \bar{\theta}_B = e.s.t.^1 \\ \theta_B = -u^0(x, 0), & \text{at } y = 0, \\ \theta_B = -\sigma_B(y) u^0(0, 0) \exp(-b_2(0, 0) y / \varepsilon), & \text{at } x = 0, \\ \theta_B = 0, & \text{at } x = 1 \text{ or } y = 1. \end{cases} \quad (2.9)$$

Similar to the process above near the boundary at $y = 0$, to balance the non-zero value $u - u^0$ at $x = 0$, we introduce the ordinary boundary layer corrector θ_L in the form,

$$\theta_L = \sigma_L(x) \bar{\theta}_L, \quad (2.10)$$

where the $\bar{\theta}_L$ is defined as a solution of

$$\begin{cases} -\varepsilon \frac{\partial^2 \bar{\theta}_L}{\partial x^2} - b_1(0, y) \frac{\partial \bar{\theta}_L}{\partial x} = 0, \\ \bar{\theta}_L = -u(0, y), & \text{at } x = 0, \\ \bar{\theta}_L \rightarrow 0, & \text{as } x \rightarrow \infty. \end{cases} \quad (2.11)$$

¹*e.s.t.* denotes a term that is exponentially small with respect to ε in the energy norm (2.2). An *e.s.t.* is negligible compared to any ε^j , $j \geq 0$.

The explicit expression of $\bar{\theta}_L$ is given by

$$\bar{\theta}_L = -u^0(0, y) \exp\left(-b_1(0, y)\frac{x}{\varepsilon}\right). \quad (2.12)$$

One can verify that the ordinary boundary layer corrector θ_L satisfies the equation,

$$\left\{ \begin{array}{l} -\varepsilon \frac{\partial^2 \theta_L}{\partial x^2} - b_1(0, y) \frac{\partial \theta_L}{\partial x} = -\varepsilon \sigma'_L \frac{\partial \bar{\theta}_L}{\partial x} - \varepsilon \sigma''_L \bar{\theta}_L - b_1(0, y) \sigma'_L \bar{\theta}_L = e.s.t., \\ \theta_L = -u^0(0, y), \quad \text{at } x = 0, \\ \theta_L = -\sigma_L(x) u^0(0, 0) \exp(-b_1(0, 0)x/\varepsilon), \quad \text{at } y = 0, \\ \theta_L = 0, \quad \text{at } x = 1 \text{ or } y = 1. \end{array} \right. \quad (2.13)$$

At this point, the difference between u and the proposed expansion $u^0 + \theta_B + \theta_L$ attains the boundary values as

$$u^\varepsilon - (u^0 + \theta_B + \theta_L) = \left\{ \begin{array}{l} -\theta_B(0, y) = \sigma_B(y) u^0(0, 0) \exp\left(-b_2(0, 0)\frac{y}{\varepsilon}\right), \quad \text{at } x = 0, \\ -\theta_L(x, 0) = \sigma_L(x) u^0(0, 0) \exp\left(-b_1(0, 0)\frac{x}{\varepsilon}\right), \quad \text{at } y = 0, \\ 0, \quad \text{at } y = 1 \text{ or } x = 1. \end{array} \right. \quad (2.14)$$

To handle the non-zero boundary values $-\theta_B$ at $x = 0$ and $-\theta_L$ at $y = 0$, appearing in (2.14), we introduce a corner corrector η in the form,

$$\eta = \sigma_L(x) \sigma_B(y) \bar{\eta}. \quad (2.15)$$

with

$$\bar{\eta} = u^0(0, 0) \exp\left(-b_1(0, 0)\frac{x}{\varepsilon}\right) \exp\left(-b_2(0, 0)\frac{y}{\varepsilon}\right). \quad (2.16)$$

The corner corrector η satisfies the equation,

$$-\varepsilon \frac{\partial^2 \eta}{\partial x^2} - \varepsilon \frac{\partial^2 \eta}{\partial y^2} - b_1(0, 0) \frac{\partial \eta}{\partial x} - b_2(0, 0) \frac{\partial \eta}{\partial y} = e.s.t. \quad (2.17)$$

Moreover, we see that the difference between u and the proposed expansion,

$$u \simeq u^0 + \theta_B + \theta_L + \eta, \quad (2.18)$$

is now finally balanced on the boundary, i.e.,

$$u - (u^0 + \theta_B + \theta_L + \eta) = 0, \quad \text{on } \partial\Omega. \quad (2.19)$$

In order to validate our asymptotic expansion of u , we introduce the difference between u and the proposed expansion,

$$w = u - (u^0 + \theta_B + \theta_L + \eta). \quad (2.20)$$

Using the equations (1.1), (2.3), (2.9), (2.13), (2.17), and (2.19), we write the equation for w ,

$$\left\{ \begin{array}{ll} -\varepsilon \Delta w - b_1 \frac{\partial w}{\partial x} - b_2 \frac{\partial w}{\partial y} = \mathcal{R}_1 + \mathcal{R}_2 + e.s.t. & \text{in } \Omega, \\ w = 0, & \text{on } \partial\Omega, \end{array} \right. \quad (2.21)$$

where

$$\mathcal{R}_1 = \varepsilon \left(\Delta u^0 + \Delta \eta + \frac{\partial^2 \theta_B}{\partial x^2} + \frac{\partial^2 \theta_L}{\partial y^2} + \Delta \eta \right), \quad (2.22)$$

$$\begin{aligned} \mathcal{R}_2 = & (b_1(x, y) - b_1(0, y)) \frac{\partial \theta_L}{\partial x} + (b_2(x, y) - b_2(x, 0)) \frac{\partial \theta_B}{\partial y} \\ & + (b_1(x, y) - b_1(0, 0)) \frac{\partial \eta}{\partial x} + (b_2(x, y) - b_2(0, 0)) \frac{\partial \eta}{\partial y}. \end{aligned} \quad (2.23)$$

Now, performing the energy estimates on the equation (2.21) and using the estimates on the correctors, we state and prove the following convergence result.

Theorem 2.1 (Non-characteristic boundary case). *Assuming the data f and \mathbf{b} are sufficiently regular, the solution u to (1.1) with $b_1, b_2 > 0$ (non-characteristic boundary case) satisfies the asymptotic expansion in (2.18) in the sense that*

$$\|u - u^0 - \theta_B - \theta_L - \eta\|_\varepsilon \leq \kappa \varepsilon^{\frac{3}{4}}. \quad (2.24)$$

Moreover, u converges to u^0 as the perturbation parameter ε tends to zero as

$$\|u - u^0\|_{L^2(\Omega)}^2 \leq \kappa \varepsilon^{\frac{1}{4}}. \quad (2.25)$$

Proof. Multiply (2.21) by $e^x w$ and integrating over Ω , we write

$$\begin{aligned} & \varepsilon \|\nabla w\|_{L^2(\Omega)}^2 + \frac{1-\varepsilon}{2} \|w\|_{L^2(\Omega)}^2 \\ & \leq \kappa \left| \int_{\Omega} [\mathcal{R}_1 + \mathcal{R}_2 + e.s.t.] w \, dx dy \right| \\ & \leq \kappa \|\mathcal{R}_1\|_{L^2(\Omega)}^2 + \kappa \|\mathcal{R}_2\|_{L^2(\Omega)}^2 + \frac{1}{4} \|w\|_{L^2(\Omega)}^2. \end{aligned} \quad (2.26)$$

Using the explicit forms of the correctors and using (2.22) and (2.23), one can verify that

$$\|\mathcal{R}_1\|_{L^2(\Omega)} \leq \kappa \varepsilon, \quad \|\mathcal{R}_2\|_{L^2(\Omega)} \leq \kappa \varepsilon^{\frac{3}{4}}. \quad (2.27)$$

Combining (2.26) and (2.27), we find that

$$\varepsilon \|\nabla w\|_{L^2(\Omega)}^2 + \frac{1}{8} \|w\|_{L^2(\Omega)}^2 \leq \kappa \varepsilon^{\frac{3}{2}}, \quad (2.28)$$

and hence we obtain (2.24). Thanks to the smallness of the correctors, (2.25) follows from (2.24), and now the proof is complete. \square

2.2. Characteristic boundary case ($b_1 > 0, b_2 = 0$). When $b_1 > 0, b_2 = 0$, the flow associated with (1.1) is moving in the x -direction across the boundary at $x = 1$. Hence, by setting $\varepsilon = 0$ in (1.1) and imposing the *inflow boundary condition* at $x = 1$, we write the equation for the limit solution u^0 as

$$\begin{cases} -b_1 \frac{\partial u^0}{\partial x} = f, & \text{in } \Omega, \\ u = 0, & \text{at } x = 1. \end{cases} \quad (2.29)$$

Since $b_1 > 0$, we find the limit solution as

$$u^0 = \int_x^1 \frac{f}{b_1}(x_1, y) dx_1. \quad (2.30)$$

The data b_1 and f are assumed to be smooth enough and hence we have the limit solution u^0 sufficiently regular for the boundary layer analysis below.

To investigate the asymptotic behavior of u^ε (solution of (1.1)) as $\varepsilon \rightarrow 0$, we first notice that $u - u^0 = 0$ on $x = 1$ only, but

$$u - u^0 \neq 0 \text{ along the boundaries at } x = 0, x = 1 \text{ and } y = 0. \quad (2.31)$$

Two different types of boundary layers occur for this interesting problem, that is, parabolic boundary layers near the top and bottom boundaries at $y = 0$ and $y = 1$, and the ordinary boundary layer near the (left) out-flow boundary at $x = 0$. Moreover, the parabolic boundary layers and the ordinary layer interact near the corners at $(0, 0)$ and $(0, 1)$. The boundary layer analysis for this characteristic boundary case is in fact very technical and complex, and it is fully analyzed in the earlier works [8, 33, 13, 14, 15].

Our main goal in this article is to construct a novel neural network, highly efficient for the singularly perturbed problem (1.1), by using the analytic information obtained from the associated boundary layer analysis. Hence we briefly recall below, especially from Section 4.1.1 in [15], the asymptotic expansion of u as well as the convergence results. The correctors introduced in this section will play an important role in Section 3.2 below when we construct our novel neural network for the singularly perturbed problem (1.1).

We construct the asymptotic expansion of u at a small ε in the form,

$$u \simeq u^0 + \varphi_B + \varphi_T + \theta_L + \zeta_B + \zeta_T, \quad (2.32)$$

where, see Fig. 2.2 below,

- u^0 : corresponding limit solution defined in (2.30),
- φ_B : parabolic boundary layer corrector (PBL) near the bottom boundary at $y = 0$,
- φ_T : parabolic boundary layer corrector (PBL) near the top boundary at $y = 1$,
- θ_L : ordinary boundary layer corrector (OBL) near the left boundary at $x = 0$,
- ζ_B : corner boundary layer corrector (CBL) that manages the interaction between φ_B and θ_L near the corner at $(0, 0)$,
- ζ_T : corner boundary layer corrector (CBL) that manages the interaction between φ_T and θ_L near the corner at $(0, 1)$.

Recalling from Section 4.1.1 in [15] that the correctors φ_B , θ_L , and ζ_B are defined as

$$\varphi_B = \sigma_B(y)\bar{\varphi}_B, \quad \text{with} \quad (2.33)$$

$$\bar{\varphi}_B = -\sqrt{\frac{2}{\pi}} \int_{(b_1(0,0)\bar{y})/\sqrt{2(1-x)}}^{\infty} \exp\left(-\frac{y_1^2}{2}\right) u^0\left(x + \frac{(b_1(0,0)\bar{y})^2}{2y_1^2}, 0\right) dy_1, \quad (2.34)$$

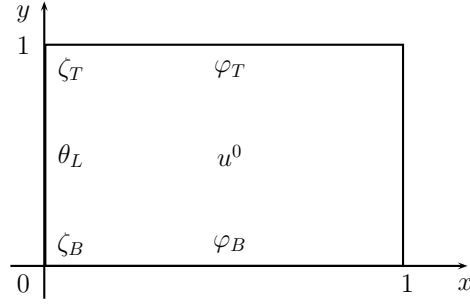


FIGURE 2.2. Limit solution, and parabolic, ordinary, and corner boundary layer correctors

where $\bar{y} = y/\sqrt{\varepsilon}$ is the stretched variable in the parabolic layer near the bottom boundary at $y = 0$, and

$$\theta_L = \sigma_L(x)\bar{\theta}_L, \quad \bar{\theta}_L = -u^0(0, y) \exp\left(-b_1(0, y)\frac{x}{\varepsilon}\right), \quad (2.35)$$

$$\zeta_B = \sigma_L(x)\sigma_B(y)\bar{\zeta}_B, \quad \bar{\zeta}_B = -\varphi_B(0, y) \exp\left(-b_1(0, y)\frac{x}{\varepsilon}\right). \quad (2.36)$$

By the symmetry, the corrector φ_T is defined by φ_B with y replaced by $1 - y$, and ζ_T by ζ_B with φ_B and y replaced by φ_T and $1 - y$.

The correctors, φ_B , θ_L , and ζ_B defined above, satisfy the equations,

$$\left\{ \begin{array}{l} -\varepsilon \frac{\partial^2 \varphi_B}{\partial y^2} - b_1(0, 0) \frac{\partial \varphi_B}{\partial x} = e.s.t., \\ \varphi_B = -u^0(x, 0), \quad \text{at } y = 0, \\ \varphi_B = \varphi_B(0, y) \neq 0, \quad \text{at } x = 0, \\ \varphi_B = 0, \quad \text{at } x = 1 \text{ or } y = 1, \end{array} \right. \quad (2.37)$$

$$\left\{ \begin{array}{l} -\varepsilon \frac{\partial^2 \theta_L}{\partial x^2} - b_1(0, y) \frac{\partial \theta_L}{\partial x} = e.s.t., \\ \theta_L = -u^0(0, y), \quad \text{at } x = 0, \\ \theta_L = -\sigma_L(x)u^0(0, 0) \exp(-b_1(0, 0)x/\varepsilon), \quad \text{at } y = 0, \\ \theta_L = 0, \quad \text{at } x = 1 \text{ or } y = 1, \end{array} \right. \quad (2.38)$$

and

$$\left\{ \begin{array}{l} -\varepsilon \frac{\partial^2 \zeta_B}{\partial x^2} - b_1(0, y) \frac{\partial \zeta_B}{\partial x} = e.s.t., \\ \zeta_B = -\varphi_B(0, y) \quad \text{at } x = 0, \\ \zeta_B = -\theta_L(x)(x, 0), \quad \text{at } y = 0, \\ \zeta_B = 0, \quad \text{at } x = 1 \text{ or } y = 1. \end{array} \right. \quad (2.39)$$

By the symmetry, the corrector φ_T satisfies the equation (2.37) of φ_B with $y = 0$ replaced by $y = 1$, and ζ_T satisfies (2.39) of ζ_B with φ_B and $y = 0$ replaced by φ_T and $y = 1$.

Thanks to our construction of the correctors, we finally notice that the difference between u and the proposed expansion is balanced on the boundary, i.e.,

$$u - (u^0 + \varphi_B + \varphi_T + \theta_L + \zeta_B + \zeta_T) = 0, \quad \text{on } \partial\Omega. \quad (2.40)$$

In order to validate our asymptotic expansion of u , we introduce the difference between u and the proposed expansion,

$$w = u - (u^0 + \varphi_B + \varphi_T + \theta_L + \zeta_B + \zeta_T), \quad (2.41)$$

and perform the energy estimates as we did in the previous section for the non-characteristic boundary case. As a result, we recall the following convergence result from Theorem 4.1 in [15]:

Theorem 2.2 (Characteristic boundary case). *Assuming the data f and \mathbf{b} are sufficiently regular, the solution u to (1.1) with $b_1 > 0$ and $b_2 = 0$ (characteristic boundary case) satisfies the asymptotic expansion in (2.32) in the sense that*

$$\|u - (u^0 + \varphi_B + \varphi_T + \theta_L + \zeta_B + \zeta_T)\|_\varepsilon \leq \kappa\varepsilon^{\frac{3}{4}}. \quad (2.42)$$

Moreover, u converges to u^0 as the perturbation parameter ε tends to zero as

$$\|u - u^0\|_{L^2(\Omega)} \leq \kappa\varepsilon^{\frac{1}{4}}. \quad (2.43)$$

Remark 2.3. The convergence rate (2.42) can be improved by imposing certain compatibility conditions on the data f . More precisely, we have:

1. If the data f satisfies $f(1, 0) = f(1, 1) = 0$, we have

$$\|u - (u^0 + \varphi_B + \varphi_T + \theta_L + \zeta_B + \zeta_T)\|_\varepsilon \leq \kappa\varepsilon.$$

2. In case when $f(x, 0) = f(x, 1) = 0$, $0 < x < 1$, then we infer from (2.30) that $u^0(x, 0) = u^0(x, 1) = 0$, and hence we do not need to include φ_B , φ_T , ζ_B , or ζ_T in our asymptotic expansion (2.32). That is, we have, for this case,

$$\|u - (u^0 + \theta_L)\|_\varepsilon \leq \kappa\varepsilon.$$

3. All the estimates above remain valid with the correctors φ , θ , and ζ replaced by their approximations without cut-off functions σ_L and σ_B denoted by $\bar{\varphi}$, $\bar{\theta}$, and $\bar{\zeta}$.

3. NUMERICAL EXPERIMENTS

For all the numerical experiments performed in this article below, we use the following setting, if not specified:

- (1) Number of epochs: EPOCHS = 1000.
- (2) Number of neurons: $n = 32$.
- (3) Loss function is defined by using the mean squared error, such as MSELoss in PyTorch.

- (4) Number of collocation points to evaluate the loss function: $N \times N$ with $N = 50$. That is, we choose $(x_i, y_j) \in \bar{\Omega}$, $i, j = 1, 2, \dots, 50$.

Our main goal in this section is to construct semi-analytic (two-layer) Physics Informed Neural Networks (PINNs) to approximate the solution u to (1.1) especially when the diffusion parameter $\varepsilon > 0$ is very small. It's important to note that our approach utilizes the two-layer neural network. This is not only computationally cost-effective but also sufficient for obtaining accurate numerical approximations. Moreover, our methodology can be conveniently expanded to an M -layer neural network by employing a symbolic computation. The detailed construction of these new semi-analytic PINNs, hereafter we call *Singular Layer PINNs* (SL-PINNs), appear below for both *characteristic* boundary and *non-characteristic* boundary cases in Sections 3.1 and 3.2, but we emphasize here that the main idea of our SL-PINNs is embedding the corrector (which describe the stiff part of the solution u) in the structure of the solution u and let the neural network learn the remaining smooth part of the solution by incorporating with the corrector. To construct our SL-PINNs, which will be verified below as highly efficient networks for (1.1) (or any other singular perturbation problems), we first recall the following two-layer (usual) PINNs:

Enforcing the zero boundary conditions to the approximation, we approximate u , sol. of (1.1), by the usual PINN approximation \tilde{u} :

$$\tilde{u}(x, y; \Theta) = x(1-x)y(1-y)\hat{u}(x, y; \Theta), \quad (\text{PINN approx. of } u), \quad (3.1a)$$

where

$$\hat{u}(x, y; \Theta) = \sum_{j=1}^n c_j \sigma(w_{1j}x + w_{2j}y + b_j), \quad n = \text{number of neurons.} \quad (3.1b)$$

The network parameters are denoted by

$$\Theta = (w_{11}, \dots, w_{1n}, w_{21}, \dots, w_{2n}, b_1, \dots, b_n, c_1, \dots, c_n),$$

and we choose the logistic sigmoid as an activation function,

$$\sigma(s) = 1/(1 + e^{-s}). \quad (3.1c)$$

As it is well-known to the community of PINNs and machine learning and as it is well-investigated in [9] for some 1D singular perturbation problems, when the singular perturbation problem (1.1) exhibits a stiff boundary layers at a small diffusivity ε , the PINN method introduced above in (3.1), (or any other version of PINNs without any special treatment near the boundary layers), fails to an approximate solution to the problem. In fact, the usual PINNs like (3.1) (with multiple layers and more neurons) do not produce a reasonable approximation to the solution of any example in the following sections when the diffusivity parameter ε is relatively smaller than the mesh size determined by the number of collocation points.

We demonstrate below how we modify the usual PINNs, \tilde{u} , in (3.1) and construct our new semi-analytic SL-PINNs for the singularly perturbed problem (1.1). That is, we enrich the PINNs with various types of boundary layer correctors as discussed in

Sections 3.1 and 3.2, depending on the nature of the boundaries, i.e., whether they are characteristic or non-characteristic.

We start with the *non-characteristic boundary case*, for which the corresponding corrector functions are given in a simpler form compared to the case of characteristic boundary case.

3.1. Non-characteristic boundary case ($b_1, b_2 > 0$). When $b_1, b_2 > 0$, i.e., the boundaries are non-characteristic, as demonstrated in Section 2.1 and supported by Theorem 2.1, the corrector functions for the boundary layers associated with (1.1) take the form of exponential functions (OBLs, CBLs) and hence they can be readily incorporated into the PINNs framework. The SL-PINNs for this non-characteristic boundary case are proposed in the following sections.

3.1.1. *Experiment 1: constant coefficients* $b_1 = b_2 = 1$. For non-characteristic boundaries, in the experiment, We consider the problem (1.1) with $b_1 = b_2 = 1$:

$$\begin{cases} -\varepsilon\Delta u - \frac{\partial u}{\partial x} - \frac{\partial u}{\partial y} = f, & \text{in } \Omega, \\ u = 0, & \text{on } \partial\Omega. \end{cases} \quad (3.2)$$

As indicated in Theorem 2.1, to absorb the sharpness of boundary layers, we write

$$u = h(x, y) - h(0, y)e^{-x/\varepsilon} + \mathcal{O}(\varepsilon), \quad (3.3a)$$

where

$$h(x, y) = u^0(x, y) - u^0(x, 0)e^{-y/\varepsilon}. \quad (3.3b)$$

To approximate the solutions u to (3.2), dropping the $\mathcal{O}(\varepsilon)$ and replacing u^0 by the neural net \hat{u} in (3.3), we propose the SL-PINN,

$$\tilde{u}(x, y) = (x - 1)(A(x, y) - A(0, y)e^{-x/\varepsilon}), \quad (3.4a)$$

$$A(x, y) = (y - 1)(\hat{u}(x, y) - \hat{u}(x, 0)e^{-y/\varepsilon}). \quad (3.4b)$$

Here, we impose the zero boundary condition to \tilde{u} at the inflows, $x = 1$ or $y = 1$.

When we compute the loss function of SL-PINNs, using the fact that

$$\sigma'(s) = \sigma(s)(1 - \sigma(s)), \quad \sigma''(s) = \sigma(s)(1 - \sigma(s))(1 - 2\sigma(s)), \quad (3.5)$$

we use the explicit form of derivatives, e.g.,

$$\begin{aligned} \frac{\partial \hat{u}}{\partial x} &= \sum_{j=1}^n c_j w_{1j} \sigma'(w_{1j}x + w_{2j}y + b_j), \\ \frac{\partial^2 \hat{u}}{\partial x^2} &= \sum_{j=1}^n c_j (w_{1j})^2 \sigma''(w_{1j}x + w_{2j}y + b_j). \end{aligned} \quad (3.6)$$

For a first example, we investigate the singular behaviors of the solutions u by computing the asymptotic errors and rates, which are shown in Table 1 and Figure 3.1. To do so, we choose $u^0 = (1 - x)(1 - y)$ as a limit solution to (3.2) for $\varepsilon = 0$,

and obtain the function $f = 2 - x - y$ accordingly. Specifically, we compute the L^2 and L^∞ norms of the asymptotic error, $u - u^0 - \bar{\theta}_B - \bar{\theta}_L - \bar{\eta}$, i.e.,

$$\tilde{u} - u^0 + u^0(0, y)e^{-x/\varepsilon} + u^0(x, 0)e^{-y/\varepsilon} - u^0(0, 0)e^{-(x+y)/\varepsilon}, \quad (3.7)$$

where \tilde{u} is from SL-PINN (3.4) and $u^0 = (1 - x)(1 - y)$. Then, the estimates for the asymptotic error (3.7) are indicated in Theorem 2.1. Figure 3.1 illustrates that the errors decrease as ε approaches zero.

	N^2	$\varepsilon = 10^{-1}$	$\varepsilon = 10^{-2}$	$\varepsilon = 10^{-3}$	$\varepsilon = 10^{-4}$
$L^2(\Omega)$	100^2	1.221×10^{-1}	2.125×10^{-3}	2.247×10^{-3}	4.869×10^{-3}
	400^2	1.529×10^{-1}	2.339×10^{-3}	1.095×10^{-3}	8.316×10^{-4}
$L^\infty(\Omega)$	100^2	4.861×10^{-1}	2.413×10^{-2}	1.016×10^{-2}	1.138×10^{-2}
	400^2	6.220×10^{-1}	2.408×10^{-2}	3.928×10^{-3}	2.6149×10^{-3}

TABLE 1. L^2 and L^∞ norms of the asymptotic error (3.7); $f = 2 - x - y$, EPOCHS = 600, $n = 32$, where N^2 is the number of collocation points.

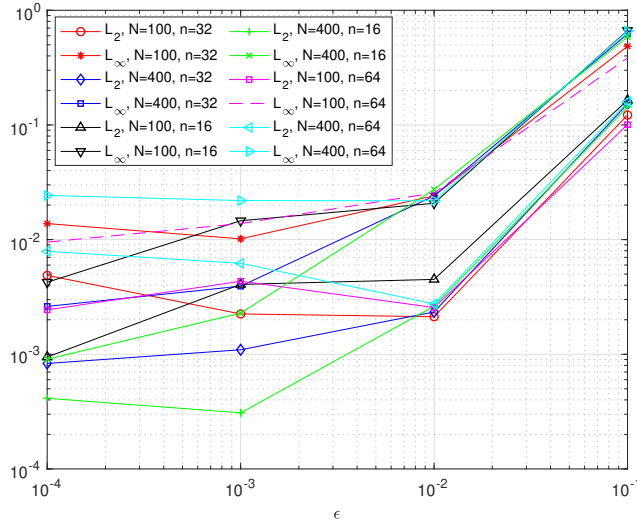
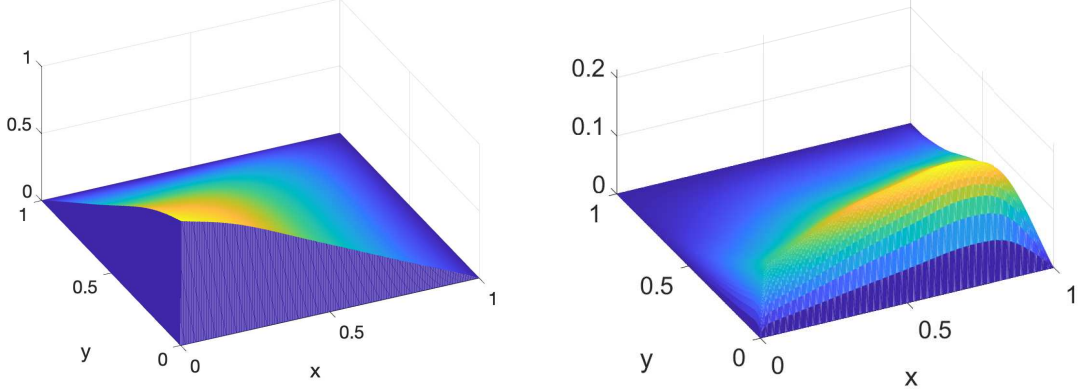


FIGURE 3.1. The $L^2(\Omega)$ and $L^\infty(\Omega)$ of (3.7) are presented with EPOCHS = 600, where n and N denote the number of neurons and collocation points, respectively. The numerical values for $n = 32$ are shown in Table 1.

For another example, we take $f = 1$. The surface plot of the corresponding solution is presented in (A), Figure 3.2 where the sharpness near the boundaries $x = 0$, or $y = 0$ are well captured.



(A) SL-PINN (3.4) for Problem (3.2)
with $f = 1$, $\varepsilon = 10^{-5}$; EPOCHS = 600

(B) SL-PINN (3.10) for Problem (3.8)
with $f = x$, $\varepsilon = 10^{-2}$; EPOCHS = 1000

FIGURE 3.2. Surface plots of SL-PINN approximations \tilde{u} .

3.1.2. *Experiment 2: variable coefficients* $b_1, b_2 > 0$. We consider the convection-diffusion equation (1.1) with $b_1 = \cos(\frac{x}{2} + y)$, $b_2 = \exp(x + y)$:

$$\begin{cases} -\varepsilon \Delta u - \cos\left(\frac{x}{2} + y\right) \frac{\partial u}{\partial x} - \exp(x + y) \frac{\partial u}{\partial y} = f, & \text{in } \Omega, \\ u = 0, & \text{on } \partial\Omega. \end{cases} \quad (3.8)$$

We notice that $b_1 = \cos(x/2 + y) > 0$ and $b_2 = \exp(x + y) > 0$ in Ω and thus, following the boundary layer analysis in Section 2.1, we find that

$$\bar{\theta}_B = -u^0(x, 0) \exp\left(-\exp(x) \frac{y}{\varepsilon}\right), \quad (3.9a)$$

$$\bar{\theta}_L = -u^0(0, y) \exp\left(-\cos(y) \frac{x}{\varepsilon}\right), \quad (3.9b)$$

$$\bar{\eta} = u^0(0, 0) \exp\left(-\frac{\cos(y)x + \exp(x)y}{\varepsilon}\right). \quad (3.9c)$$

As done in (3.3) and (3.4), we use the corrector functions above and propose the SL-PINN as

$$\tilde{u}(x, y) = (x - 1) \left(A(x, y) - A(0, y) \exp(-\cos(y)x/\varepsilon) \right), \quad (3.10a)$$

$$A(x, y) = (y - 1) \left(\hat{u}(x, y) - \hat{u}(x, 0) \exp(-\exp(x)y/\varepsilon) \right). \quad (3.10b)$$

The surface plot of solution to (3.8) for $f = x$ is shown in (B), Figure 3.2. The sharpness of the solutions near the boundaries are well captured.

Now we move to the more interesting *characteristic boundary case*.

3.2. Characteristic boundary case ($b_1 > 0, b_2 = 0$). As we observed in Section 2.2, the small parameter $\varepsilon > 0$ in the equation (1.1) results in the formation of parabolic boundary layers (PBLs, φ_B and φ_T) along the characteristic boundaries at $y = 0$ and $y = 1$. In fact, it is more difficult, and on the other hand more interesting, to embedding these parabolic correctors in the structure of PINN approximations than the other simpler ordinary corrector and corner correctors. Hence, as a first step, we consider the case of compatible data f , satisfying $f(x, 0) = f(x, 1) = 0$, for which the parabolic boundary layers (nor the corner layers) do not occur; see Remark 2.3. As a result, we only incorporate the correctors for OBLs ($\bar{\theta}$ of θ) in the neural network approximations, as shown in Section 2.2 below. In the following section, Section 3.2.2, we also examine the case of non-compatible f , which may not satisfy $f(x, 0) = 0$ or $f(x, 1) = 0$. In this case, we anticipate the formation of the PBLs and corner boundary layers (CBLs, $\bar{\zeta}_B$ of ζ_B and $\bar{\zeta}_T$ of ζ_T) at the intersection of the OBLs and PBLs.

3.2.1. *Experiment 3: compatible f s.t. $f(x, 0) = f(x, 1) = 0$.* We consider the equation (1.1) with $b_1 = 1, b_2 = 0$ and $f(x, 0) = f(x, 1) = 0$:

$$\begin{cases} -\varepsilon\Delta u - \frac{\partial u}{\partial x} = f, & \text{in } \Omega, \\ u = 0, & \text{on } \partial\Omega. \end{cases} \quad (3.11)$$

Since $\bar{\varphi}_B = \bar{\varphi}_T = \bar{\zeta}_B = \bar{\zeta}_T = 0$, as indicated in Remark 2.3, we write

$$u = u^0(x, y) - u^0(0, y)e^{-x/\varepsilon} + \mathcal{O}(\varepsilon). \quad (3.12)$$

We thus approximate the solution u to (3.11) by the SL-PINN,

$$\tilde{u}(x, y) = (x - 1)y(y - 1)(\hat{u}(x, y) - \hat{u}(0, y)e^{-x/\varepsilon}). \quad (3.13)$$

For the experiment, we take $f = \sin(\pi y)$ which is compatible at $y = 0, 1$, i.e., $f(x, 0) = f(x, 1) = 0$.

For the comparison purpose, we use the exact solution to (3.11),

$$u(x, y) = (Ae^{r^+x} + Be^{r^-x} + \frac{1}{\varepsilon\pi^2})\sin(\pi y) \quad (3.14a)$$

where

$$A = \frac{e^{r^-} - 1}{\varepsilon\pi^2(e^{r^+} - e^{r^-})}; \quad B = \frac{1 - e^{r^+}}{\varepsilon\pi^2(e^{r^+} - e^{r^-})}; \quad r^\pm = \frac{1}{2\varepsilon}(-1 \pm \sqrt{1 + 4\varepsilon^2\pi^2}). \quad (3.14b)$$

We obtain the numerical errors $u - \tilde{u}$ in $L^2(\Omega)$ and $L^\infty(\Omega)$ as shown in Table 2. We also plot them in Figure 3.4.

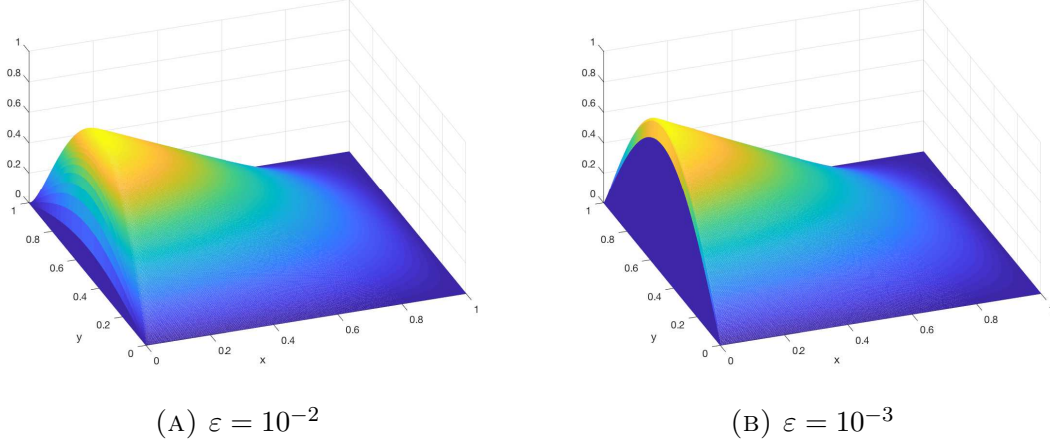


FIGURE 3.3. The surface plots of the neural net approximation \tilde{u} by SL-PINN (3.13) for Problem (3.11) with $f = \sin(\pi y)$.

	N^2	$\varepsilon = 10^{-1}$	$\varepsilon = 10^{-2}$	$\varepsilon = 10^{-3}$	$\varepsilon = 10^{-4}$	$\varepsilon = 10^{-5}$
$\ u - \tilde{u}\ _{L^2(\Omega)}$	100^2	1.350×10^{-4}	2.404×10^{-4}	1.693×10^{-3}	1.019×10^{-3}	3.933×10^{-3}
	400^2	1.538×10^{-4}	1.531×10^{-4}	7.894×10^{-4}	2.457×10^{-3}	3.566×10^{-4}
$\ u - \tilde{u}\ _{L^\infty(\Omega)}$	100^2	3.552×10^{-4}	7.675×10^{-4}	6.210×10^{-3}	3.355×10^{-3}	1.229×10^{-2}
	400^2	3.688×10^{-4}	4.002×10^{-4}	2.965×10^{-3}	7.644×10^{-3}	1.186×10^{-3}

TABLE 2. L^2 and L^∞ errors ($\|u - \tilde{u}\|_{L^2(\Omega)}$ and $\|u - \tilde{u}\|_{L^\infty(\Omega)}$) for SL-PINN (3.13) and Problem (3.11) with $f = \sin(\pi y)$.

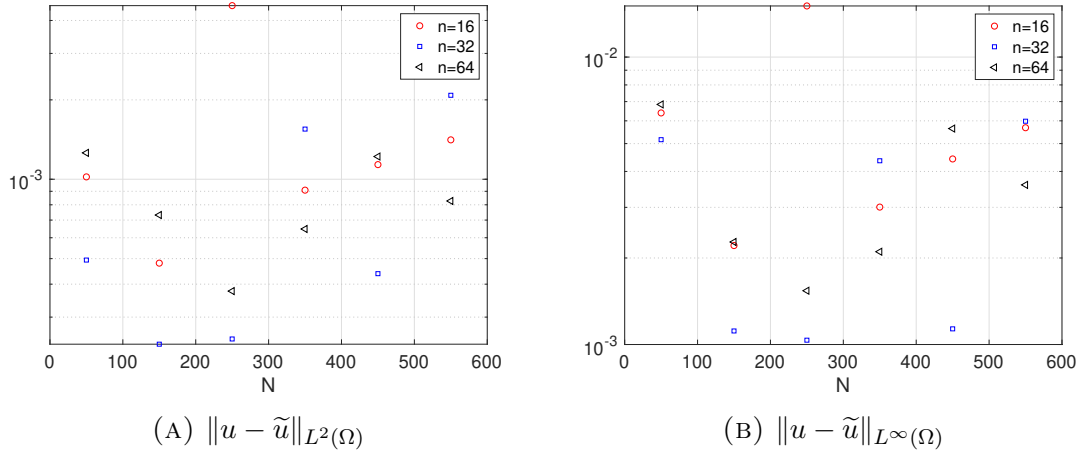


FIGURE 3.4. SL-PINN (3.13) for Problem (3.11) with $f = \sin(\pi y)$, $\varepsilon = 10^{-3}$; the number of neurons = $n = 16, 32, 64$; N^2 is the number of collocation points.

As we see in Figure 3.4, it is evident that if the neural network size is too large ($n = 64$), the network results in poor interpolation between the collocation points. Conversely, if the network size is too small ($n = 16$), it fails to capture the sharpness of the solutions, leading to poor interpolation results. Optimal performance is achieved when $n = 32$, resulting in lower L^2 and L^∞ errors compared to the other network sizes.

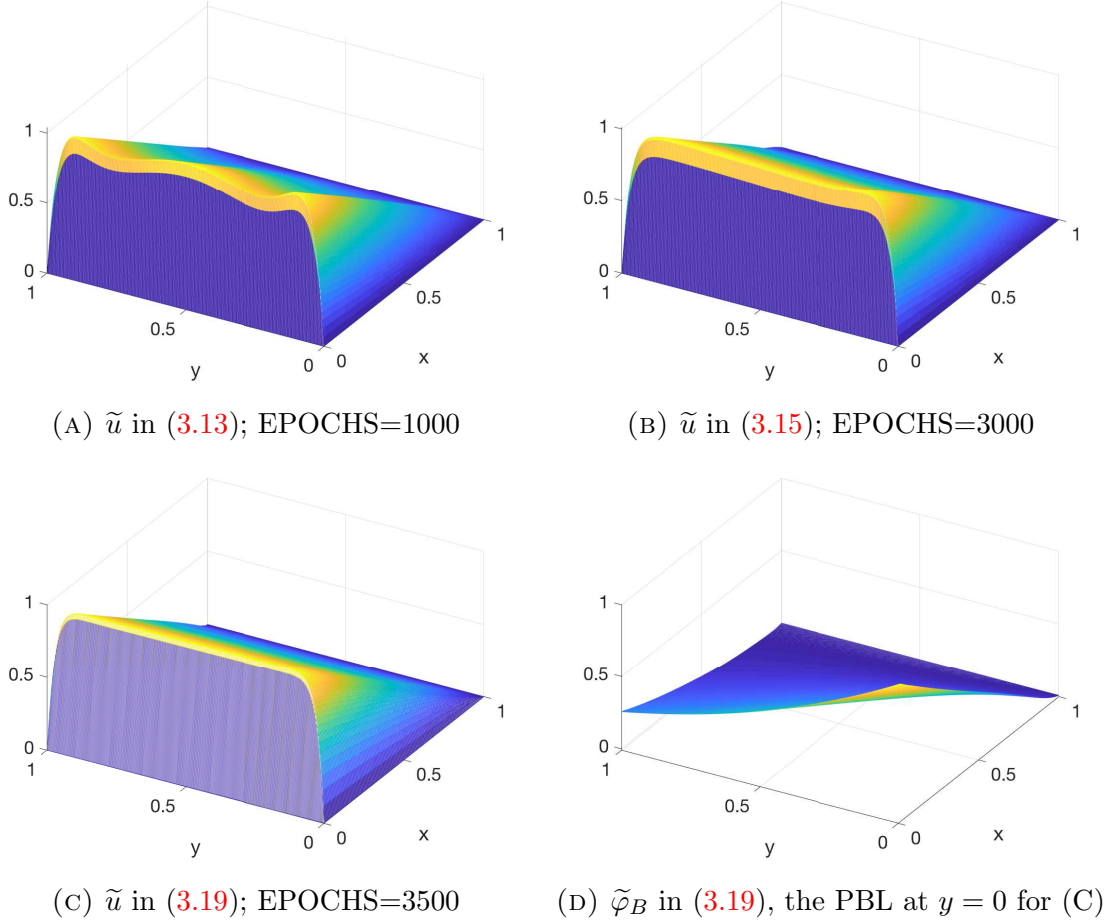


FIGURE 3.5. The surface plots of the neural net approximation \tilde{u} for Problem (3.11) with $f = 1, \varepsilon = 10^{-3}$; The number of EPOCHS is chosen to ensure convergence in stochastic optimization.

3.2.2. *Experiment 4: non-compatible f , i.e., $f(x, 0) \neq 0$ or $f(x, 1) \neq 0$.* If we use the SL-PINN (3.13) for the non-compatible f , as in Figure 3.5 - (A), we observe the large over-shootings near the edges $y = 0, 1$. As indicated in Theorem 2.2, it is due to the parabolic boundary layers (PBLs) and near the corners $(0, 0), (0, 1)$ due to the corner layers (CBLs).

As our *first* and *simple* try to resolve the large computational error of the SL-PINN (3.13) near the edges $y = 0, 1$, we introduce the simple exponentially decaying

functions, $e^{-y/\sqrt{\varepsilon}}$ and $e^{-(1-y)/\sqrt{\varepsilon}}$ near $y = 0, 1$, and construct the following SL-PINN enriched with those functions:

$$\tilde{u}(x, y) = (x - 1) (A(x, y) - A(0, y) e^{-x/\varepsilon}), \quad (3.15a)$$

$$A(x, y) = \hat{u}(x, y) - \hat{u}(x, 0)(1 - y)e^{-y/\sqrt{\varepsilon}} - \hat{u}(x, 1)ye^{-(1-y)/\sqrt{\varepsilon}}, \quad (3.15b)$$

Compared to the PBLs $\bar{\varphi}_B$ in (2.34), these empirically obtained exponential functions are preferred due to their simplicity of implementation using the exponential functions and their ability to effectively capture the sharpness of the layers. However, as seen in Figure 3.5 (B), we still observe small over-shootings near $(0, 0)$ and $(0, 1)$, indicating that the empirically obtained exponential functions do not fully capture the sharpness of the PBLs and CBLs.

In order to fully account for the small over-shootings and achieve a sharp approximation, we require the use of all the PBLs $\bar{\varphi}_B$, $\bar{\varphi}_T$, the CBLs $\bar{\zeta}_B$, $\bar{\zeta}_T$, and the OBL $\bar{\theta}_L$. As indicated in Remark 2.3 for non-compatible f , we write

$$u = h(x, y) - h(0, y)e^{-x/\varepsilon} + \mathcal{O}(\varepsilon^{\frac{3}{4}}), \quad (3.16a)$$

where

$$h(x, y) = u^0(x, y) - \bar{\varphi}_B(x, y) - \bar{\varphi}_T(x, y). \quad (3.16b)$$

To construct the SL-PINN, we drop the $\mathcal{O}(\varepsilon^{\frac{3}{4}})$, replace u^0 with the neural net approximation \hat{u} , and write the SL-PINN approximation \tilde{u} as

$$\tilde{u}(x, y) = (x - 1) (A(x, y) - A(0, y) e^{-x/\varepsilon}), \quad (3.17a)$$

$$A(x, y) = \hat{u}(x, y) - \bar{\varphi}_B(x, y) - \bar{\varphi}_T(x, y), \quad (3.17b)$$

where the heat solutions $\bar{\varphi}_B$ and $\bar{\varphi}_T$ are defined in (2.34). Because these parabolic correctors are involved in convolution integrals, implementing SL-PINN with those correctors is not practical nor convenient.

As an alternative, we propose to construct the SL-PINN for the following system of equations for u , $\bar{\varphi}_B$ and $\bar{\varphi}_T$ all together:

$$-\varepsilon \Delta u - \frac{\partial u}{\partial x} = f, \quad \text{in } \Omega, \quad (3.18a)$$

$$-\frac{\partial^2 \bar{\varphi}_B}{\partial y^2} - \frac{\partial \bar{\varphi}_B}{\partial x} = 0, \quad \text{in } \Omega, \quad (3.18b)$$

$$-\frac{\partial^2 \bar{\varphi}_T}{\partial y^2} - \frac{\partial \bar{\varphi}_T}{\partial x} = 0, \quad \text{in } \Omega, \quad (3.18c)$$

$$(3.18d)$$

supplemented with the boundary conditions

$$u = 0 \text{ on } \partial\Omega, \quad (3.18e)$$

$$\bar{\varphi}_B(x, 0) = -u^0(x, 0), \quad \bar{\varphi}_B(1, y) = 0, \quad \bar{\varphi}_B \rightarrow 0 \text{ as } y \rightarrow \infty, \quad (3.18f)$$

$$\bar{\varphi}_T(x, 1) = -u^0(x, 1), \quad \bar{\varphi}_T(1, y) = 0, \quad \bar{\varphi}_T \rightarrow 0 \text{ as } y \rightarrow -\infty. \quad (3.18g)$$

To approximate $\bar{\varphi}_B, \bar{\varphi}_T$, we respectively use the neural net approximations $\tilde{\varphi}_B, \tilde{\varphi}_T$,

$$\tilde{\varphi}_B = (x - 1)(e^{-\tilde{y}}\hat{u}(x, 0) + (e^{-\tilde{y}} - e^{-2\tilde{y}})\hat{\varphi}_B), \quad (3.19a)$$

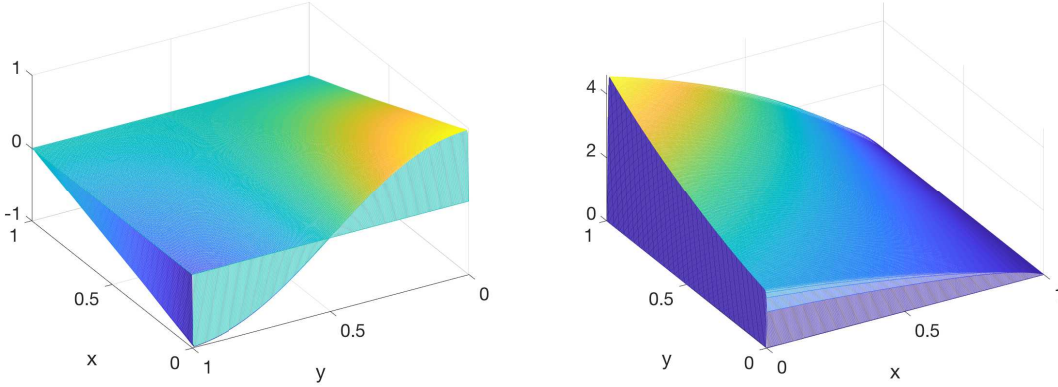
$$\tilde{\varphi}_T = (x - 1)(e^{-\tilde{y}}\hat{u}(x, 1) + (e^{-\tilde{y}} - e^{-2\tilde{y}})\hat{\varphi}_T), \quad (3.19b)$$

and, to approximate the solution u , we use \tilde{u} :

$$\tilde{u}(x, y) = A(x, y) - A(0, y)(1 - x)e^{-x/\varepsilon}, \quad (3.19c)$$

$$A(x, y) = (x - 1)\hat{u}(x, y) - (1 - y)\tilde{\varphi}_B - y\tilde{\varphi}_T. \quad (3.19d)$$

Figure 3.5, (D) shows the neural net approximation $\tilde{\varphi}_B$, while the $\tilde{\varphi}_T$ can be shown similarly. By utilizing the corrector functions, $\tilde{\varphi}_B, \tilde{\varphi}_T$, as shown in (C), we can accurately approximate the solution u by \tilde{u} in (3.19). As opposed to (A) and (B), no over-shootings are observed at the corners $(0, 0)$, $(0, 1)$ or the edges $y = 0, 1$.



(A) $f = \cos(\pi y)$, $\varepsilon = 10^{-6}$; EPOCHS=3500, $N^2 = 50^2$ (B) $f = \exp(x + y)$, $\varepsilon = 10^{-5}$; EPOCHS=3500, $N^2 = 350^2$

FIGURE 3.6. The surface plot of the neural net approximation \tilde{u} by SL-PINN (3.19) for Problem (3.11).

For more non-compatible examples, we consider the functions $f = \cos(\pi y)$ and $\exp(x + y)$. The neural net solutions \tilde{u} by the SL-PINN in (3.19), depicted in Figure 3.6, agree with the numerical solutions in [21]. To achieve higher accuracy in (B), we require a larger number of collocation points, specifically $N = 350$.

In future work, we will investigate a system similar to (3.18) for more general problems involved in various boundary layers in different locations and their interactions.

4. CONCLUSION

In this study, we have introduced a semi-analytic method, called SL-PINN, to enhance the numerical efficiency of 2-layer PINNs when solving singularly perturbed boundary value problems, convection-dominated equations on rectangular domains. For each problem, we obtained an analytic approximation of the stiff component of

the solution within the boundary layer, referred to as the *corrector* function. Incorporating the correctors into the structure of the 2-layer PINNs, we resolved the stiffness issue of the approximate solutions and developed a new semi-analytic SL-PINNs enriched with the correctors. Through numerical simulations in Section 3, we confirmed that our new approach produces stable and convergent approximations of the solutions.

ACKNOWLEDGMENTS

Gie was partially supported by Ascending Star Fellowship, Office of EVPRI, University of Louisville; Simons Foundation Collaboration Grant for Mathematicians; Research R-II Grant, Office of EVPRI, University of Louisville; Brain Pool Program through the National Research Foundation of Korea (NRF) (2020H1D3A2A01110658). Hong was supported by Basic Science Research Program through the National Research Foundation of Korea (NRF) funded by the Ministry of Education (NRF-2021R1A2C1093579) and the Korea government(MSIT)(No. 2022R1A4A3033571). Jung was supported by the National Research Foundation of Korea(NRF) grant funded by the Korea government(MSIT) (No. 2023R1A2C1003120).

REFERENCES

- [1] Arzani, Amirhossein; Cassel, Kevin W.; D’Souza, Roshan M. Theory-guided physics-informed neural networks for boundary layer problems with singular perturbation. *J. Comput. Phys.* 473 (2023), Paper No. 111768, 15 pp. [3](#)
- [2] J. Berg and K. Nystrom. A unified deep artificial neural network approach to partial differential equations in complex geometries. *Neurocomputing*, 317 (2018), pp. 28–41. [2](#)
- [3] J. Blechschmidt, O. G. Ernst. Three ways to solve partial differential equations with neural networks—a review. *GAMM-Mitteilungen*, 44 (2) (2021). [2](#)
- [4] Yuan Cao, Zhiying Fang, Yue Wu, Ding-Xuan Zhou, and Quanquan Gu. Towards Understanding the Spectral Bias of Deep Learning. *Proceedings of the Thirtieth International Joint Conference on Artificial Intelligence*, 8 (2021). [3](#)
- [5] Z. Chen, V. Churchill, K. Wu, D. Xiu. Deep neural network modeling of unknown partial differential equations in nodal space. *Journal of Computational Physics* 449 (2022). [2](#)
- [6] Junho Choi, Chang-Yeol Jung, and Hoyeon Lee. On boundary layers for the Burgers equations in a bounded domain. *Commun. Nonlinear Sci. Numer. Simul.*, 67:637–657, 2019. [2](#)
- [7] Olga Fuks and Hamdi A Tchelepi. Limitations of physics informed machine learning for non-linear two-phase transport in porous media. *Journal of Machine Learning for Modeling and Computing*, 1(1), 2020. [3](#)
- [8] P. Grisvard. *Elliptic problems in nonsmooth domains*, volume 69 of 261 Classics in Applied Mathematics. Society for Industrial and Applied 262 Mathematics (SIAM), Philadelphia, PA, 2011. Reprint of the 1985 263 original. [3](#), [8](#)
- [9] G.-M. Gie, Y. Hong, and C.-Y. Jung. Semi-analytic PINN methods for singularly perturbed boundary value problems *Submitted*. [3](#), [11](#)
- [10] G.-M. Gie, C.-Y. Jung, and H. Lee. Enriched Finite Volume approximations of the plane-parallel flow at a small viscosity. *Journal of Scientific Computing*, 84, 7 (2020). [2](#)
- [11] G.-M. Gie, C.-Y. Jung, and H. Lee. Semi-analytic time differencing methods for singularly perturbed initial value problems. *Numerical Methods for Partial Differential Equations*, 38, 5, 1367 - 139, 2022. [2](#)

- [12] G.-M. Gie, C.-Y. Jung, and H. Lee. Semi-analytic shooting methods for Burgers' equation. *Journal of Computational and Applied Mathematics*, Vol. 418, 2023, Article 114694. **2**
- [13] Gung-Min Gie, Chang-Yeol Jung, and Roger Temam. Analysis of mixed elliptic and parabolic boundary layers with corners. *Int. J. Differ. Equ.*, pages Art. ID 532987, 13, 2013. **3, 8**
- [14] Gung-Min Gie, Chang-Yeol Jung, and Roger Temam. Recent progresses in boundary layer theory. *Discrete and Continuous Dynamical Systems - Series A*, Vol. 36, no. 5, 2016, 2521–2583. **3, 8**
- [15] G.-M. Gie, M. Hamouda, C.-Y. Jung, and R. Temam, *Singular perturbations and boundary layers*, volume 200 of *Applied Mathematical Sciences*. Springer Nature Switzerland AG, 2018. <https://doi.org/10.1007/978-3-030-00638-9> **2, 3, 8, 10**
- [16] H. Han and R. B. Kellogg, *A method of enriched subspaces for the numerical solution of a parabolic singular perturbation problem*. In: *Computational and Asymptotic Methods for Boundary and Interior Layers*, Dublin, pp.46-52 (1982). **2**
- [17] J. Han, Y. Lee. Hierarchical learning to solve partial differential equations using physics-informed neural networks. *arXiv preprint*, arXiv:2112.01254 (2021). **2**
- [18] M. H. Holmes, *Introduction to perturbation methods*, Springer, New York, 1995. **2**
- [19] Youngjoon Hong, Chang-Yeol Jung, and Jacques Laminie. Singularly perturbed reaction-diffusion equations in a circle with numerical applications. *Int. J. Comput. Math.*, 90(11):2308–2325, 2013. **2**
- [20] Youngjoon Hong, Chang-Yeol Jung, and Roger Temam. On the numerical approximations of stiff convection-diffusion equations in a circle. *Numer. Math.*, 127(2):291–313, 2014. **2**
- [21] Chang-Yeol Jung and Roger Temam. Numerical approximation of two-dimensional convection-diffusion equations with multiple boundary layers. *International Journal of Numerical Analysis and Modeling*. Vol. 2, no. 4, 2005. **19**
- [22] G. E. Karniadakis, I. G. Kevrekidis, L. Lu, P. Perdikaris, S. Wang, L. Yang. Physics-informed machine learning. *Nature Reviews Physics*, 3 (6) (2021) 422–440. **2**
- [23] E. Kharazmi, Z. Zhang, G. E. Karniadakis. Variational physics-informed neural networks for solving partial differential equations. *arXiv preprint*, arXiv:1912.00873 (2019). **2**
- [24] E. Kharazmi, Z. Zhang, and G. E. Karniadakis. hp-VPINNs: Variational physics-informed neural networks with domain decomposition. *Comput. Methods in Appl. Mech. Eng.*, 374 (2021). **2**
- [25] Zongyi Li and Hongkai Zheng and Nikola Kovachki and David Jin and Haoxuan Chen and Burigede Liu and Kamyar Azizzadenesheli and Anima Anandkumar, Physics-Informed Neural Operator for Learning Partial Differential Equations *arXiv: 2111.03794*, (2022). **3**
- [26] I.E. Lagaris, A. Likas, and D.I. Fotiadis. Artificial neural networks for solving ordinary and partial differential equations. *IEEE Trans Neural Netw.*, 1998;9(5):987-1000. **2**
- [27] R. E. O'Malley, *Singularly perturbed linear two-point boundary value problems*. SIAM Rev. **50** (2008), no. 3, pp 459-482. **2**
- [28] Nasim Rahaman, Aristide Baratin, Devansh Arpit, Felix Draxler, Min Lin, Fred Hamprecht, Yoshua Bengio, and Aaron Courville. On the Spectral Bias of Neural Networks. *Proceedings of the 36th International Conference on Machine Learning*, 97 (2019). **3**
- [29] M. Raissi and G. E. Karniadakis. Hidden physics models: machine learning of nonlinear partial differential equations. *J. Comput. Phys.*, 357 (2018), pp. 125–141. **2**
- [30] M. Raissi, P. Perdikaris, and G. E. Karniadakis. Physics-informed neural networks: a deep learning framework for solving forward and inverse problems involving nonlinear partial differential equations. *J. Comput. Phys.*, 378 (2019), pp. 686–707. **2**
- [31] S. H. Rudy, S. L. Brunton, J. L. Proctor, J. N. Kutz. Data-driven discovery of partial differential equations. *Science advances*, 3 (4) (2017). **2**
- [32] Maziar Raissi, Alireza Yazdani, and George Em Karniadakis. Hidden fluid mechanics: Learning velocity and pressure fields from flow visualizations. *Science*, 367(6481), pp.1026–1030, 2020. **3**

- [33] S. Shih and R. B. Kellogg, *Asymptotic analysis of a singular perturbation problem*. SIAM J. Math. Anal. **18** (1987), pp . 1467-1511. [2](#), [3](#), [8](#)
- [34] J. Sirignano, K. Spiliopoulos. Dgm: A deep learning algorithm for solving partial differential equations. *Journal of computational physics*, 375 (2018) 1339–1364. [2](#)
- [35] Mario De Florio, Enrico Schiassi, and Roberto Furfaro. Physics-informed neural networks and functional interpolation for stiff chemical kinetics. *Chaos* 32, 063107 (2022). [2](#)
- [36] Sifan Wang, Yujun Teng, and Paris Perdikaris. Understanding and mitigating gradient flow pathologies in physics-informed neural networks. *SIAM Journal on Scientific Computing*, 43(5):A3055–A3081, 2021. [3](#)

¹ DEPARTMENT OF MATHEMATICS, UNIVERSITY OF LOUISVILLE, LOUISVILLE, KY 40292

² DEPARTMENT OF MATHEMATICAL SCIENCES, KOREA ADVANCED INSTITUTE OF SCIENCE AND TECHNOLOGY

³ DEPARTMENT OF MATHEMATICAL SCIENCES, ULSAN NATIONAL INSTITUTE OF SCIENCE AND TECHNOLOGY, ULSAN 44919, KOREA

Email address: gungmin.gie@louisville.edu

Email address: hongyj@kaist.ac.kr

Email address: cjung@unist.ac.kr

Email address: tmunkhjin@unist.ac.kr